Available online at www.sciencedirect.com
ScienceDirect
Journal of Computational Physics 218 (2006) 102–122
JOURNAL OF COMPUTATIONAL PHYSICS
www.elsevier.com/locate/jcp

Particle-in-cell method for parallel dynamics in magnetized electron plasmas: Study of high-amplitude BGK modes

F. Peinetti [a], F. Peano [a], G. Coppa [a,*], J. Wurtele [b]

[a] *Dipartimento di Energetica, Politecnico di Torino, Corso Duca degli Abruzzi 24, 10129 Torino, Italy*
[b] *Department of Physics, UC Berkeley and Center for Beam Physics, LBNL, Berkeley, CA 94720, United States*

Received 24 October 2005; received in revised form 28 December 2005; accepted 27 January 2006
Available online 13 March 2006

Abstract

The present paper describes the numerical technique that has been developed, in the framework of the particle-in-cell (PIC) method, to study the dynamics of a nonneutral plasma along the magnetic field lines. In particular, the technique has been employed to simulate the formation and long-term evolution of large-amplitude electrostatic waves experimentally observed in electron plasmas confined in a Penning trap [W. Bertsche, J. Fajans, L. Friedland, Phys. Rev. Lett. 91 (2003) 265003]. Due to the peculiar features of the physical system, namely the existence of different time scales and the presence of a perturbative oscillating potential, ad hoc numerical techniques have been developed. In particular, with a suitable radial decomposition all important two-dimensional phenomena are fully taken into account while keeping the computational effort to that of a standard one-dimensional PIC codes. Moreover, a novel particle loading technique (ergodic loading) has been developed, which ensures a significant reduction of numerical noise. The results obtained with the present technique are in excellent agreement with the experiments [F. Peinetti, W. Bertsche, J. Fajans, J. Wurtele, L. Friedland, Phys. Plasmas 12 (2005) 062112]. Moreover, results presented here furnish clear evidences of the close relationship between the observed nonlinear structures and the Bernstein–Greene–Kruskal modes.

PACS: 52.65.Rr; 52.27.Jt

Keywords: Plasma physics; Nonneutral plasmas; Particle-in-cell techniques; BGK modes

1. Introduction

Pure electron plasmas have drawn considerable attention over the last 15 years. In fact, the possibility of long-time confinement in Penning traps has made these plasmas very attractive for investigations of a wide range of different fields in physics, including basic plasma physics [1–5], Eulerian fluid dynamics [6–9], and anti-matter experiments [10,11].

* Corresponding author. Tel.: +39 011 564 4419; fax: +39 011 564 4499.
E-mail address: gianni.coppa@polito.it (G. Coppa).

0021-9991/$ - see front matter
doi:10.1016/j.jcp.2006.01.040

In the last years, many experimental and theoretical works pointed out the analogies between nonneutral plasmas and nonlinear oscillators, in particular exploring the employment of autoresonance (adiabatic nonlinear phase locking and synchronization) in the excitation and control of several nonlinear features of these systems. In particular, recent experiments [1] showed the possibility of inducing large-amplitude density oscillations in a pure electron plasma confined in a Penning trap by means of a weak, oscillating external drive of adiabatically-decreasing frequency. Using this technique, density fluctuations slowly emerge from the background and can reach amplitudes of order of the nominal plasma density, presenting clear evidence of a well-localized structure bouncing back and forth in the trap. The density oscillations are not damped once the external drive is switched off, but persist for tens of thousands of oscillations. The plot of a typical process of formation and growth of these structures is seen in Fig. 1. Fig. 1(a) shows the time behavior of the external potential which drives the plasma oscillations; note the downward chirp of the drive frequency. Fig. 1(b) shows the time behavior of the plasma density obtained with the code here presented (the density has been averaged radially, and is evaluated at an axial position close to one of the two end electrodes): one sees that the density fluctuations associated with the emerging structure slowly increase, over many bounce periods, when the drive is on. These slowly-growing density oscillations are consistent with the presence, inside the plasma, of a well-localized structure, moving back and forth along the plasma column and slowly growing in amplitude. As soon as the drive is switched off, the density fluctuations stop growing, but the constant-amplitude fluctuations in the undriven evolution of the plasma show that the structure is well preserved for many bounce periods. As collisions are negligible on the time scale of interest, these highly-stable nonlinear structures must be stationary solutions of the Vlasov equation and, to all extents, they represent the first experimental evidence of high-amplitude Bernstein–Greene–Kruskal (BGK) modes [12] in a laboratory plasma.

The numerical investigation of the phenomenon proves challenging: in fact, the observed nonlinear structures are induced by small-amplitude oscillations of an external, perturbing potential and they evolve on a time scale much slower than the characteristic time scale of the thermal electron motion inside the trap. Moreover, the details of the interaction between the particles and the external drive on the faster time scale are crucial for the generation of the long-term effects observed in the experiments. In principle, the numerical analysis of these slowly-emerging nonlinear structures could have been performed using a three-dimensional particle-in-cell code [13]. Nonetheless, the remarkable computational effort required by such an approach would have

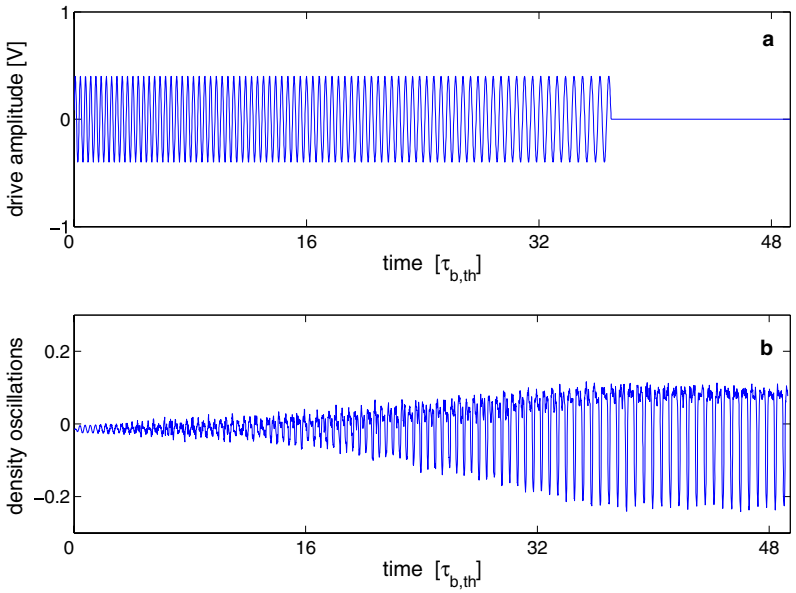

Fig. 1. (a) Plot of the time behavior of the external potential which drives the plasma oscillation. The drive is switched off at $t/\tau_{b,th} = 37$, where $\tau_{b,th}$ is the bounce period for the axial motion of a thermal electron. (b) Calculated evolution of the plasma density fluctuations. When the drive is turned off, the amplitude of the oscillations stops growing and quickly reaches a stationary value, thus showing that the structure induced by the drive is well preserved in the undriven evolution of the plasma.

been unjustified: as explained in the following, the interesting kinetic features of the phenomenon under consideration are essentially one-dimensional, even though two-dimensional effects need be included in order to perform reliable simulations of the experiments. For these reasons, an ad hoc particle-in-cell method has been developed with appropriate numerical features for the simulation of the phenomenon with high accuracy, which helps provide deeper physical insights into the dynamics of formation and growth of the structures observed in the experiments. Results obtained with the code, which have been published previously [14], are in remarkable quantitative agreement with the experimental data. In the present paper, the details of the original numerical techniques implemented in the code are presented: the techniques have been developed for this specific case, but they can be of interest for other applications in computational plasma physics.

The paper is organized as follows: in Section 2, the kinetic model for the description of the system under consideration is presented, and the more relevant issues to be accounted for in the numerical solution of this model are discussed; in Section 3, the numerical model, along with the numerical methods, are presented, while Section 4 describes an innovative loading algorithm which allowed for a significant reduction of the noise in the simulations. In Section 5, tests on the validity of the algorithm are reported, while typical results attainable with the code are presented in Section 6; in particular, results providing further information about the nature of these nonlinear structures are reported in Section 6.2, showing the close connections between these objects and the theory of the Bernstein–Greene–Kruskal modes.

2. Mathematical model and relevant numerical considerations

A Penning trap is composed of a sequence of hollow cylindrical gates, biased at different potentials (a schematic plot is in Fig. 2). The axial confinement of the pure electron plasma is provided by an electrostatic potential well, created after the injection of the plasma, by grounding the central electrodes and properly biasing the end electrodes at a negative potential, $-V_0$. The radial confinement is provided by a uniform, axial magnetic field that inhibits any radial particle transport on the time scale of interest for the experiments. The plasma is located at the bottom of the potential well, with electrons bouncing back and forth in the axial direction and moving slowly in the azimuthal direction because of $\vec{E} \times \vec{B}$ drift.

The formation of the nonlinear structures observed in the experiments is inherently related to deep modifications of the phase-space structure of the plasma, which, at the end of the driving process, is far from Maxwellian [15]. Hence, the nature of the phenomenon is intrinsically kinetic, with no fluid limit, and its full theoretical description requires a two-dimensional kinetic treatment of the plasma, in terms of the Vlasov–Poisson model. Due to the intensity of the magnetic field, the Larmor radius of the electrons is much smaller than any relevant length scale and a gyrokinetic approximation can be invoked for the electron motion in the (r, θ) transverse plane. Under this hypothesis, the Vlasov equation reads:

$$\frac{\partial f}{\partial t} + \frac{1}{Br}\left(\frac{\partial \Phi}{\partial r}\frac{\partial f}{\partial \theta} - \frac{\partial \Phi}{\partial \theta}\frac{\partial f}{\partial r}\right) + v_z\frac{\partial f}{\partial z} + \frac{e}{m_e}\frac{\partial \Phi}{\partial z}\frac{\partial f}{\partial v_z} = 0 \tag{1}$$

where f is the electron phase-space distribution function (i.e., $f(r,\theta,z,v_z,t)r\,\mathrm{d}r\,\mathrm{d}\theta\,\mathrm{d}z\,\mathrm{d}v_z$ is the number of electrons with position between r and $r + \mathrm{d}r$, z and $z + \mathrm{d}z$, θ and $\theta + \mathrm{d}\theta$, and with axial velocity between v_z and $v_z + \mathrm{d}v_z$). In the cases considered here, in which the plasma distribution is azimuthally symmetric, the second term in Eq. (1), describing the dynamics induced by the $\vec{E} \times \vec{B}$ drift, vanishes, as $\partial/\partial\theta = 0$ for both f and Φ. Under this hypothesis, the axial magnetic field, while leaving the z-dynamics unaffected, inhibits any radial

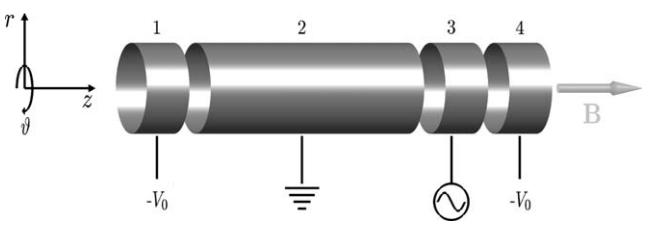

Fig. 2. Schematic view of a Penning trap, showing the electrodes biased at different potentials (1–2 and 4 at fixed biases) and the drive electrode, (3), biased at a small, oscillating potential. A coil wound around the electrodes creates the axial, static magnetic field $\vec{B}$ which is responsible for the radial confinement of the plasma.

dynamics on the time scales of interest. Consequently, the system of equations governing the evolution of the system can be simplified to

$$\begin{cases} \dfrac{\partial f}{\partial t} + v_z \dfrac{\partial f}{\partial z} + \dfrac{e}{m_e} \dfrac{\partial \Phi}{\partial z} \dfrac{\partial f}{\partial v_z} = 0, \\ \Phi = \varphi + \sum\limits_j \phi^{(j)}, \\ \nabla^2 \varphi = \dfrac{e}{\varepsilon_0} \displaystyle\int f \, \mathrm{d}v_z, \\ \varphi(r = R_w) = 0, \\ \dfrac{\partial \varphi}{\partial z}(z = z_a, z_b) = 0, \\ f(r, z, v_z, t = 0) = \left(\dfrac{m_e}{2\pi k T_e}\right)^{1/2} g(r) \exp\left[-\dfrac{m_e v_z^2/2 - e\Phi(r, z, t = 0)}{k T_e}\right], \end{cases} \tag{2}$$

where $f = f(r, z, v_z, t)$. In the equations, R_w is the radius of the trap and z_a, z_b are the axial coordinates defining the z boundaries of the trap. The reduced form of the Vlasov equation shows that the electron dynamics is substantially one-dimensional, with the dependence on the radial coordinate essentially parametric. Therefore, the plasma can be regarded as a set of one-dimensional distributions, positioned at different radii and interacting only through the self-consistent potential generated by the plasma. The electrostatic potential $\Phi(r,z,t)$ is the sum of the self-consistent potential $\varphi(r,z,t)$ and the potential generated by each electrode of the trap. In general, the potential generated by the jth electrode (see Fig. 2) is determined by solving the Laplace equation,

$$\nabla^2 \phi^{(j)} = 0, \tag{3}$$

with proper boundary conditions:

$$\phi^{(j)}(r = R_w, z, t) = \begin{cases} V^{(j)}(t), & z \in [z_{1,j}, z_{2,j}], \\ 0, & z \notin [z_{1,j}, z_{2,j}], \end{cases} \tag{4}$$

and

$$\frac{\partial \phi^{(j)}}{\partial z}(r, z = z_a, z_b) = 0, \tag{5}$$

where $z_{1,j}$, $z_{2,j}$ are the axial positions delimiting the jth electrode, and $V^{(j)}$ is the biasing potential. In the schematic view of the trap of Fig. 2, and for the experiments discussed above, one has

$$\begin{cases} V^{(1)} = V^{(4)} = -V_0, \\ V^{(2)} = 0, \\ V^{(3)} = V_\mathrm{d} \sin \psi_\mathrm{d}(t), \end{cases} \tag{6}$$

where, of course, $\phi^{(2)} \equiv 0$ and ψ_d, the drive phase, is frequency-chirped such that

$$\frac{\mathrm{d}\psi_\mathrm{d}}{\mathrm{d}t} = \omega_\mathrm{d}(t) = \omega_0 - \alpha t. \tag{7}$$

It should be remarked that the boundary conditions for $z = z_a$ and z_b are not rigorous. However, more sophisticated boundary conditions would lead to solutions that are appreciably different only for z close to z_a and z_b, while the fields are practically indistiguishable in the region of interest occupied by the plasma. For this reason, the simplest boundary condition, $\partial\Phi/\partial z = 0$, has been used for both the Poisson and the Laplace equations.

Finally, the sixth of Eq. (2) defines the initial distribution for the Vlasov–Poisson system: a Boltzmann equilibrium distribution is assumed, as the Boltzmann hypothesis holds in (z, v_z) space, at each radius [8,9,14]. This is justified by the presence of the strong axial magnetic field, which allows for the thermalization process to occur only along the magnetic field lines. The function $g(r)$ defines the radial profile of the distribution function and depends, in general, on the way electrons are loaded inside the Penning trap. In fact, the initial density profile is

$$n_0(r,z) = \int f_0(r,z,v_z)\,\mathrm{d}v_z = g(r)\exp\left(\frac{e\Phi}{kT_e}\right) \tag{8}$$

hence, in setting the initial conditions, one can define the desired radial profile for either the density field in the center of the trap, $n(r,z=0)$, or for the z-integrated density, $\sigma(r)$ [9]. In the first case, one has

$$g(r) = n_c(r)\exp\left(-\frac{e\Phi_c(r)}{kT_e}\right), \tag{9}$$

where $\Phi_c(r)$ is the radial profile of the total potential in the central region of the trap (where it does not depend on z), while in the second case

$$g(r) = \frac{\sigma(r)}{\mathscr{L}(r)}, \tag{10}$$

where $\mathscr{L}(r) = \int_{z_a}^{z_b} \exp(e\Phi/kT_e)\,\mathrm{d}z$ is the effective length of the plasma column at radius r.

The numerical integration of Vlasov–Poisson models (such as that of Eq. (2)) is commonly carried out using particle-in-cell techniques, which have proven to be powerful and versatile tools for the numerical investigation of plasmas [16,17]. However, due to the nature of the problem under consideration, the use of some ad hoc numerical schemes, which differ from those adopted in a standard PIC algorithm, allows efficient and precise PIC simulations of the experiments with a reduced computational cost, affordable even on a single-processor computer.

The simulation must model the interaction of the plasma with a weak, localized oscillating potential with an adiabatically-varying frequency. In general, the perturbing potential induces small modifications in the electrons trajectories during a single bounce; nonetheless, large modifications to the unperturbed motion of the resonant electrons are expected over a time during which the drive frequency varies appreciably [15]. Hence, the drive introduces two well-defined time scales in the system. The faster time scale is the period of the drive, $2\pi/\omega_d(t)$ ($\omega_d(t)$ is the instantaneous drive frequency, Eq. (7)), which is of the order of the thermal bounce period of the electrons in the axial potential well, $\tau_{b,th} \simeq 2\pi/\omega_d$. The second, slower time scale is characterized by the time τ_s over which relevant changes of ω_d are to be expected, $\tau_s \simeq \omega_0/\alpha$ (being $\alpha = \dot{\omega}_d$ the frequency sweep rate, according to Eq. (7)) [1]. The phenomenon of the formation and growth of these nonlinear structures occurs on the slower time scale, and in the experiments, typically, $\tau_s/\tau_b \sim 10^2$–10^3. As the excitation process is based on the autoresonant phase synchronization between the drive and the electrons of the plasma, the motion of the electrons must be followed accurately for many bounce periods, so as not to alter the phase relations between drive and particles. As a consequence, the crucial role of the numerical noise in these simulations has to be remarked. It is well-known that the control of the noise is a fundamental issue in PIC codes, but it is of particular relevance here, as it can hamper the excitation of the structures observed in the experiments. In fact, if the noise in the self-consistent potential is of the order of the external drive, no real excitation occurs in the system, hence no structure is induced in the plasma. In practice, for the noise level to be tolerable, the inequality $\left|\frac{\phi_{drive}}{\varphi}\right| \gg \left|\frac{\delta\phi_{noise}}{\varphi}\right|$ must hold, where, typically, one has $\left|\frac{\phi_{drive}}{\varphi}\right| \lesssim 10^{-2}$. Thus, one must resort to numerical techniques aimed at reducing the level of numerical noise in the simulations. For this purpose, the choice of the algorithm adopted for the initial loading of the particle distribution has proven to be primarily important. A novel loading technique has been developed, which represents an extension of classic loading techniques [16]. The algorithm reproduces an ergodic distribution of the computational particles on different energies and allows a significant reduction of the numerical noise for the cases of interest.

3. Numerical model of the system

Altough the experiments have been given a theoretical interpretation and qualitative comparisons can be obtained on the basis of one-dimensional analytical models [15], an accurate quantitative comparison requires a more realistic two-dimensional modelization of the system. In fact, two-dimensional effects are important in the evaluation of the electric fields acting on the plasma, especially when the radius of the plasma column is comparable with the trap radius. Nonetheless, following the discussion of the previous section, a fully two-dimensional simulation of the system is unnecessary as long as the shape of the axial potential well (and of

the perturbing drive) is evaluated accurately inside the trap. Moreover, two-dimensional simulations may prove computationally expensive because of the presence of the above mentioned different time scales in the system, especially if one is interested in studying the plasma response for a wide range of driving conditions. For this reason, in order to speed up the calculations, and on the basis of the observations previously derived, a simple method for the radial decomposition of the system has been employed. The basic idea of the algorithm is to consider the plasma as a superposition of N_R one-dimensional systems, each of which represents a certain "radial layer" inside the plasma. By doing so, the two-dimensional distribution function of Eq. (2) decouples as follows:

$$f(r,z,v_z,t) \simeq \sum_{k=1}^{N_R} f_k(z,v_z,t) S_k(r), \tag{11}$$

where the shape function for the kth layer, S_k, defined as

$$S_k(r) = \frac{1}{2\pi r_k \Delta r_k} b_0\left(\frac{r-r_k}{\Delta r_k}\right), \tag{12}$$

is a normalized b_0-spline function associated with the kth radial zone. In Eq. (12), r_k and Δr_k are the mean radius and the width of the kth radial zone, respectively, and the support of the functions $\{S_k\}$ are nonoverlapping and adjacent to one another.

In the radial decomposition, Eq. (11), the most convenient number of radial zones, N_R, can be determined on the basis of the computational cost and the required accuracy. Several criteria are possible in the choice of the quantities $\{r_k\}$ and $\{\Delta r_k\}$ ($k = 1, \ldots, N_R$) of Eq. (12). Hence, it is useful to determine a procedure to find the best representation of a generic radial profile by means of a piecewise-constant function with a given number of radial zones, N_R, which must be regarded as an input parameter for the PIC simulations. In this section, the numerical algorithm descending from the hypothesis of Eq. (11) is presented for a generic radial decomposition. A detailed discussion of the procedure adopted in the discretization of the plasma radial profile is reported separately in Appendix A.

A three-dimensional sketch of the approximation induced in the system by the radial decomposition of Eq. (11) is shown, in Fig. 3, for a reference case in which a Gaussian profile has been discretized with $N_R = 5$ radial zones. The figure shows the results for the phase-space (z, v_z) density in the three radial zones. The hole in phase space created by the drive is visible, at different radii, in the lower part of the figure.

According to the normalization of Eq. (12), one has

$$2\pi \int_0^{R_w} S_k(r) r \, \mathrm{d}r = 1 \quad k = 1, \ldots, N_R. \tag{13}$$

This corresponds to splitting the real plasma distribution into N_R annular distributions, to be regarded as one-dimensional objects. By inserting Eq. (11) into the first Eq. (2), multiplying by $S_n(r)$ and integrating in $r\,\mathrm{d}r$, one obtains

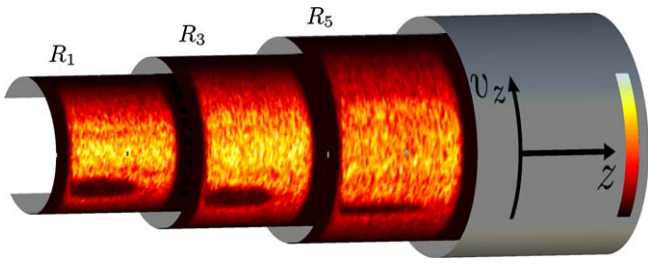

Fig. 3. Structure of nested sheets corresponding to the radial decomposition of Eq. (11): five radial zones have been employed in the calculations, and a subset of three radial zones is plotted.

$$\frac{\partial f_n}{\partial t} + v_z \frac{\partial f_n}{\partial z} + \frac{e}{m_e} \frac{\partial \overline{\Phi}_n}{\partial z} \frac{\partial f_n}{\partial v_z} = 0 \quad n = 1, \ldots, N_R, \tag{14}$$

where $\overline{\Phi}_n(z,t)$ is the radial average of the two-dimensional electrostatic potential over the nth radial zone:

$$\overline{\Phi}_n(z,t) = \frac{1}{r_n \Delta r_n} \int_{\Delta r_n} \Phi(r,z,t) r \, \mathrm{d}r = \overline{\varphi}_n(z,t) + \sum_j \overline{\phi}_n^{(j)}(z,t). \tag{15}$$

In this way, the dynamics has been completely averaged over the generic radial zone: in fact, all the quantities in Eq. (15) depend only on z. The total potential appearing in Eq. (15) is the sum of the potentials due to the electrodes and of the self-consistent potential. The radial averages $\overline{\phi}_n^{(j)}$ are carried out once, at the beginning of the calculations; on the contrary, the average of the self-consistent field must be performed at each time step, after solving the Poisson equation:

$$\frac{1}{r} \frac{\partial}{\partial r} \left(r \frac{\partial \varphi}{\partial r} \right) + \frac{\partial^2 \varphi}{\partial z^2} = \frac{e}{\varepsilon_0} \sum_{k=1}^{N_R} \left[\int f_k(z, v_z, t) \, \mathrm{d}v_z \right] S_k(r). \tag{16}$$

Given the geometry and the boundary conditions of the system, a Bessel decomposition can be conveniently considered for the self-potential (in which the first N_B radial eigenfunctions are retained):

$$\varphi(r,z,t) \simeq \sum_{h=1}^{N_B} \varphi_h(z,t) J_0 \left(\frac{j_{0,h}}{R_w} r \right), \tag{17}$$

in this way, the two-dimensional Poisson equation is reduced to a set of one-dimensional, second-order differential equations, of the form

$$\frac{\partial^2 \varphi_h}{\partial z^2} - \left(\frac{j_{0,h}}{R_w} \right)^2 \varphi_h = \frac{e}{\varepsilon_0} \sum_{k=1}^{N_R} \left[\int f_k(z, v_z, t) \, \mathrm{d}v_z \right] C_{h,k} \quad h = 1, \ldots, N_B, \tag{18}$$

in which the set of Bessel coefficients for the plasma radial profile (see Eqs. (11) and (12))

$$C_{h,k} = \frac{1}{\pi r_k \Delta r_k R_w^2 J_1^2(j_{0,h})} \int_{\Delta r_k} J_0 \left(\frac{j_{0,h}}{R_w} r \right) r \, \mathrm{d}r \tag{19}$$

is evaluated at the beginning of the simulation. After solving the set of Eq. (18), the quantity $\overline{\varphi}_n$ of Eq. (15) can be evaluated as

$$\overline{\varphi}_n = \frac{1}{r_n \Delta r_n} \sum_{h=1}^{N_B} \varphi_h(z,t) \int_{\Delta r_n} J_0 \left(\frac{j_{0,h}}{R_w} r \right) r \, \mathrm{d}r. \tag{20}$$

The quantities $N_k = \{ \int \int f_k(z, v_z, t) \, \mathrm{d}z \, \mathrm{d}v_z \}_{k=1,\ldots,N_R}$ are constant in time, as they represent the total number of electrons within each radial zone.

The radial decomposition described above requires special attention into the initial conditions, as the equilibrium configuration for the plasma consistent with Eqs. (11), (14), (15), and (16) is not obvious. In fact, as the radial average of quantities obtained from two-dimensional calculations has been defined above, one might consider determining the initial conditions by averaging, over the different radial zones, the distribution obtained from the solution of the two-dimensional, nonlinear Poisson equation

$$\nabla^2 \Phi(r,z) = \frac{e}{\varepsilon_0} g(r) \exp \left(\frac{e \Phi(r,z)}{k T_e} \right), \tag{21}$$

which defines the equilibrium configuration for the fully two-dimensional problem (see Eqs. (8)–(10)). Actually, this procedure is not consistent with the radial approximation employed here. In fact, recalling Eqs. (11)–(15), a consistent equilibrium density profile must follow the Boltzmann distribution when the radially-averaged total potential of Eq. (15) is considered on each radial zone, that is

$$n_h(z) = n_{h,0} \exp \left(\frac{e \overline{\Phi}_h(z)}{k T_e} \right) \tag{22}$$

and the corresponding phase-space distribution in the nth layer can be written as

$$f_h(z, v_z) = n_h(z)\left(\frac{m}{2\pi k T_e}\right)^{1/2} \exp\left(-\frac{m v_z^2}{2kT}\right). \tag{23}$$

In this way, the initial phase-space distribution is not exactly the zonal average of the equilibrium distribution function for the fully two-dimensional problem, even if the difference between the two quantities decreases when N_R is increased. If the initial phase-space distribution for the generic zone, Eq. (23), were of the form

$$f_h(z, v_z) = \left(\frac{m}{2\pi k T_e}\right)^{1/2} \exp\left(-\frac{m v_z^2}{2kT}\right) \frac{1}{r_h \Delta r_h} \int_{\Delta r_h} g(r) \exp\left(\frac{e\Phi(r,z)}{kT_e}\right) r \, \mathrm{d}r, \tag{24}$$

the initial conditions would not be exactly in equilibrium, and small re-arrangements of the phase-space plasma distribution would occur during the early phase in the evolution of the system.

Thus, the two-dimensional density field must be written as

$$n(r,z) = \sum_{h=1}^{N_R} n_{h,0} \exp\left(\frac{e\overline{\Phi}_h}{kT_e}\right) b_0\left(\frac{r - r_h}{\Delta r_h}\right) \tag{25}$$

and the initial equilibrium distribution is obtained by solving the nonlinear Poisson equation for the total potential,

$$\nabla^2 \Phi(r,z) = \frac{e}{\varepsilon_0} \sum_{h=1}^{N_R} n_{h,0} \exp\left(\frac{e\overline{\Phi}_h(z)}{kT_e}\right) b_0\left(\frac{r - r_h}{\Delta r_h}\right), \tag{26}$$

which provides, through Eqs. (22) and (15), the initial conditions for each radial zone.

Eq. (26) can be solved efficiently with a semi-implicit, iterative method, in which the $(n+1)$th iteration of the potential, $\Phi^{(n+1)}$, is calculated by solving a linearized version of Eq. (26), obtained by rewriting the RHS of Eq. (26) as

$$\sum_{h=1}^{N_R} n_{h,0} \exp\left(\frac{e\overline{\Phi}_h^{(n+1)}(z)}{kT_e}\right) b_0\left(\frac{r - r_h}{\Delta r_h}\right) \simeq \left[1 + \frac{e\delta\Phi^{(n)}(r,z)}{kT_e}\right] \sum_{h=1}^{N_R} n_{h,0} \exp\left(\frac{e\overline{\Phi}_h(z)^{(n)}}{kT_e}\right) b_0\left(\frac{r - r_h}{\Delta r_h}\right), \tag{27}$$

where

$$\delta\Phi^{(n)}(r,z) = \Phi^{(n+1)}(r,z) - \Phi^{(n)}(r,z). \tag{28}$$

4. Ergodic loading

In general, loading the initial distribution of computational particles in phase-space is a delicate part of a PIC algorithm, as it can deeply affect the noise level of the simulations. For this reason, a proper particle loading can allow for a significant reduction in the number of computational particles necessary to achieve a tolerable noise level. As the computational cost of the code is roughly proportional to the number of particles, good particle loading can increase the speed of the calculations.

The problem of particle loading has been studied extensively [16]. The loading techniques referred to as quiet starts usually allow for noise levels which are much lower than those achievable by means of algorithms based on the generation of random numbers. A common case is that of a uniform plasma, in which the computational particles are usually loaded on a proper set of cold beams, and then the initial particle positions are suitably defined in order to reduce correlations between particles (for example, the reversed two-bit loading [16]). Then, the weights of the particles are adjusted in order to reproduce the desired velocity distribution. This approach may not, however, be the best choice when the initial conditions are defined by a plasma in equilibrium with spatially-varying fields, as in the present case, where the plasma is initially confined by an electrostatic potential well, in thermal equilibrium with the potential Φ. The density profile of Eq. (8) is, in general, roughly constant in the center of the trap and falls to zero abruptly near the end electrodes, on a length scale of the order of the radius of the trap. The total potential $\Phi(z)$ is almost independent of z in

the central part of the trap, and the loading techniques discussed previously are well suited for this region. Nonetheless, care must be taken when loading the particles at the ends of the plasma column. In fact, the potential has rapid spatial variation at the ends of the trap. If the same sampling in velocity is employed in the center and at the end of the plasma column, higher energies are sampled at the ends of the plasma column with respect to the central region. As a consequence, in the early stage of the simulation, particles initially at the ends of the plasma column, while moving toward the center of the trap, soon overtake those initially positioned further away from the column ends, thus creating unphysical density fluctuations. In the simulations, these density spikes, which are evident at the beginning of the evolution, are usually partially phase-mixed in a time of the order of the thermal bounce period. Nonetheless, a rather high level of noise is observed as a consequence of this initial disturbance. A large number of computational particles would be required to reduce this effect so that the plasma dynamics with a weak external drive can be studied.

An example of density fluctuations is shown in Fig. 4, where the undriven evolution of an initial equilibrium distribution is plotted, in the case of $N_P = 2.5 \times 10^4$ particles and for a single radial zone. The phase-space distribution and the density profile are shown at different times in the very early stage of the evolution (i.e., for $t \lesssim \tau_b$). The figure shows that the loaded distribution is indeed near equilibrium, but the dynamics of particles initially at the ends of the plasma column lead to the formation of density spikes due to a z-dependent sampling of the energy distribution. At the beginning, these fluctuations are localized and do not affect the density profile in the center of the trap, which is still flat. Nonetheless, at later times, the disturbance propagates

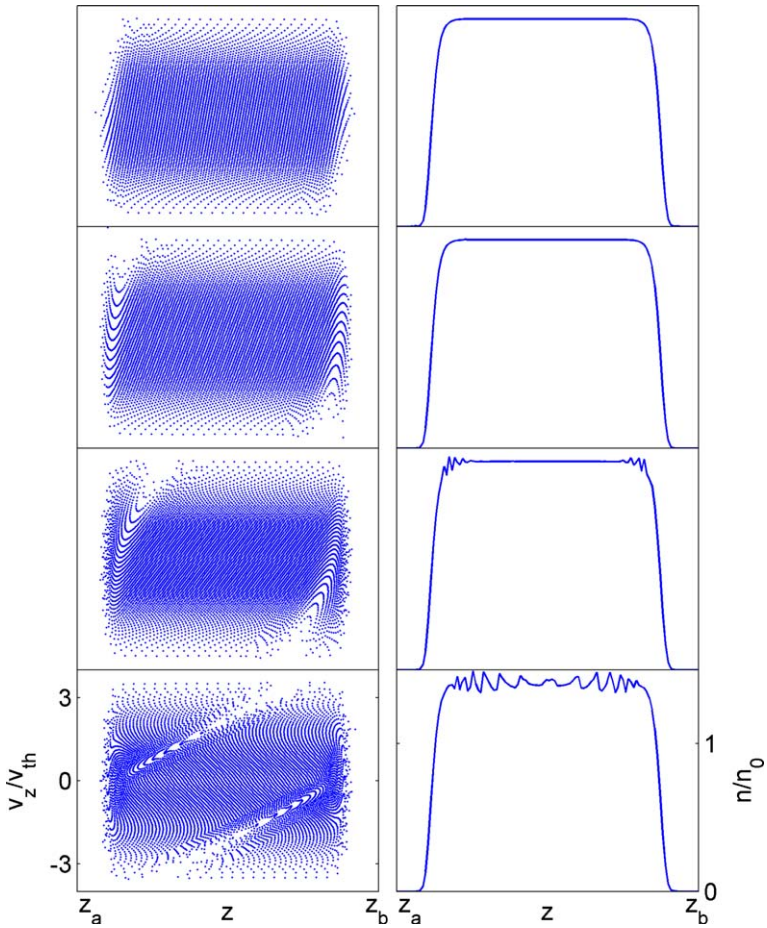

Fig. 4. Evolution of the phase-space plasma distribution at times smaller than the thermal electron bounce period, and corresponding radially-averaged density profiles (the simulations uses 2.5×10^4 computational particles, with only a representative subset of the distribution shown in the plots).

towards the center, leading to fluctuations in the whole domain. In this particular example, the effect of the classic loading procedure is particularly evident because of the relatively small number of computational particles. However, this feature becomes particularly relevant when either large sweep-rates are employed (as a nonnegligible part of the sweep occurs when the nonphysical density spikes are still present) or very small drive amplitudes are considered (as, in this case, noise has to be kept to very small levels).

A large improvement in noise reduction (and, hence, in computational efficiency) has been obtained with a different loading technique, henceforth referred to as ergodic loading. In general, an equilibrium distribution can be written as

$$f_{0,j}(z, v_z) = F_j(H_j(z, v_z)), \tag{29}$$

where $H_j(z,v_z)$ is the electron axial Hamiltonian for the jth radial layer:

$$H_j(z, v_z) = \frac{1}{2} m v_z^2 - e\overline{\Phi}_j(z). \tag{30}$$

When an initial Maxwellian distribution is considered, the function F_j has the form

$$F_j(\epsilon) \propto \mathrm{e}^{-\frac{\epsilon}{kT_e}}. \tag{31}$$

In general, the function F_j is different from the particle energy density, ρ_j. In fact, the energy density can be calculated from the electron distribution function by observing that

$$\rho(\epsilon) = \int\int f_0(z, v_z)\delta[H(z, v_z) - \epsilon]\,\mathrm{d}z\,\mathrm{d}v_z = F(\epsilon)\int\int \delta[H(z, v_z) - \epsilon]\,\mathrm{d}z\,\mathrm{d}v_z = F(\epsilon)\frac{\tau(\epsilon)}{m_e}, \tag{32}$$

(the subscript j is dropped for the sake of simplicity), where $\tau(\epsilon)$ is the bounce period of an electron of energy ϵ in the equilibrium potential:

$$\tau(\epsilon) = \oint \sqrt{\frac{m_e}{2(\epsilon + e\Phi(z))}}\,\mathrm{d}z. \tag{33}$$

On the other hand, the initial phase-space distribution can be written in terms of $\rho(\epsilon)$ as

$$f_0(z, v_z) = \int F(\epsilon)\delta[H(z, v_z) - \epsilon]\,\mathrm{d}\epsilon = \int \rho(\epsilon)\frac{\delta[H(z, v_z) - \epsilon]}{\int\int \delta\left[H\left(z', v_z'\right) - \epsilon\right]\mathrm{d}z'\,\mathrm{d}v_z'}\,\mathrm{d}\epsilon. \tag{34}$$

The fraction in Eq. (34) can be interpreted as the probability of being at (z, v_z) for an electron bouncing in the potential well with energy ϵ. According to the ergodic theory, this quantity can be rewritten in the form

$$\frac{1}{\tau(\epsilon)}\int_0^{\tau(\epsilon)} \delta(z - z(t;\epsilon))\delta(v_z - v_z(t;\epsilon))\,\mathrm{d}t, \tag{35}$$

where $z(t;\epsilon)$ and $v_z(t;\epsilon)$ define the closed phase-space trajectory of the electron at the considered energy ϵ. Eq. (35) can be discretized as

$$\frac{1}{N_t(\epsilon)}\sum_{\alpha=1}^{N_t(\epsilon)} \delta[z - z(t_\alpha(\epsilon);\epsilon)]\delta[v_z - v_z(t_\alpha(\epsilon);\epsilon)] \tag{36}$$

by considering $N_t(\epsilon)$ points on the trajectory, uniformly distributed in time within the bounce period $\tau(\epsilon)$, i.e., $t_\alpha(\epsilon) = \alpha \times \tau(\epsilon)/N_t(\epsilon)$.

In this way, the initial electron distribution function $f_0(z, v_z)$ can be approximated as

$$f_0(z, v_z) \simeq \sum_{\beta=1}^{N_\epsilon}\sum_{\alpha=1}^{N_t(\epsilon_\beta)} \frac{\rho(\epsilon_\beta)\Delta\epsilon_\beta}{N_t(\epsilon_\beta)}\delta[z - z(t_\alpha(\epsilon_\beta);\epsilon_\beta)]\delta[v_z - v_z(t_\alpha(\epsilon_\beta);\epsilon_\beta)]. \tag{37}$$

Eq. (37) is the procedure followed in ergodic loading: the initial distribution is approximated by properly loading a set of suitably-weighted computational particles on the phase-space trajectories corresponding to a predefined set of energies $\{\epsilon_\beta\}$. At first, the trajectory and the corresponding bounce period (Eq. (33)) are

calculated for each energy ϵ_β: then, $N_t(\epsilon_\beta)$ equally-weighted computational particles are positioned on the trajectory according to Eq. (37), i.e., uniformly distributed in time (see Fig. 5).

It is worth observing that the procedure illustrated here is equivalent to loading the plasma distribution on a proper set of cold beams in the (Θ,J) space, where

$$J(\epsilon) = \oint m v_z(\epsilon, z)\,\mathrm{d}z \tag{38}$$

is the action and Θ the conjugated angle. Thus, if a spatially-varying equilibrium potential is present in the initial distribution, the classic loading algorithm can still be employed, but must be carried out in the (Θ,J) space and then must be followed by a mapping to the (z, v_z) space.

Different options are possible when choosing the set of energies $\{\epsilon_\beta\}$ and the number of particles to be positioned at each energy level, $N_t(\epsilon_\beta)$, the choice being problem-dependent. In any case, it was observed that a fine energy sampling is required at lower energies in order to achieve very low noise levels. In fact, as the potential has very small gradients in the center of the trap, trajectories corresponding to close values of energy may differ significantly at the turning points. As the particles are positioned on phase-space trajectories, the procedure described above may lead to unsatisfactory filling of phase-space regions at very low values of v_z. Moreover, this technique allows for a good sampling of particles in particular regions of velocity space, for example where oscillating fields may be resonant with particles. In the experiments described here, this region is, initially, in the tail of the distribution [1,15].

In the following simulations, the parameter $N_t(\epsilon)$ has been kept constant but, as in the standard loading techniques, this is not the only possible choice. For instance, another procedure may consist of placing different number $N_t(\epsilon_\beta)$ of computational particles in each energy interval proportional to the fraction of real particles in $\Delta\epsilon_\beta$,

$$N_t(\epsilon_\beta) \simeq \frac{\rho(\epsilon_\beta)\Delta\epsilon_\beta}{\int \rho(\epsilon)\,\mathrm{d}\epsilon} N_P, \tag{39}$$

where N_P is the total number of computational particles employed in the simulation.

The density evolution for the case of Fig. 4, performed with the same number of computational particles but with the new loading technique, is shown in Fig. 6. In the figure, the plots refer to times corresponding to the first and last distribution of Fig. 4; the initial distribution is preserved with high precision and the improvement in terms of noise reduction is clearly visible.

The ergodic loading technique allows for a very smooth and accurate description of the early stage of the excitation (when a resonant population of electrons is forming in the tail of the Maxwellian distribution), allowing for a noise reduction which is remarkable if compared to conventional loading schemes. As shown in Fig. 7, in which the time evolution of the density is plotted, in the case of conventional loading (Fig. 7(a))

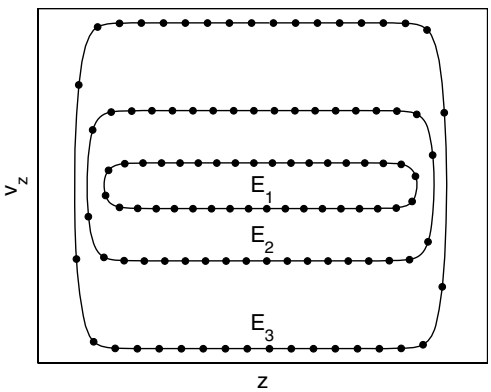

Fig. 5. Phase-space trajectories for three different values of the energy, $E_1 < E_2 < E_3$, and corresponding initial positions for computational particles. For each energy level, the distribution follows an ergodic hypothesis, i.e., particles are equally spaced in time within the (energy-dependent) bounce period.

...nent in Fig. 4, with
...consisting of 30 energy

zones, N_R, and the total number of computational particles, N_P, in order to check the efficiency of the numerical algorithm. Fig. 8 shows results from a parametric study, in which the plasma response has been computed for different combinations of N_R and N_P in the ranges $N_R = 1$–5 and $N_P = 3.7 \times 10^4 - 3 \times 10^5$. In the figure, the mean oscillation amplitude of the plasma density at a fixed axial position and averaged radially, $\langle \mathscr{A} \rangle$, obtained by averaging $\mathscr{A}$ over 20 undriven bounce periods, is plotted with its standard deviation, $\sigma_{\mathscr{A}}$. It has to be remarked that $\sigma_{\mathscr{A}}$ is not expected to vanish even for large values of N_P, because the amplitude fluctuations cannot be totally ascribed to purely-numerical issues: in fact, the drive contains a high number of spatial harmonics (as in the experiments) and, therefore, higher-order drive-plasma resonances are present, which are responsible for the formation of smaller structures and for density oscillations of low amplitude [15]. Nonetheless, a contribution to the fluctuations is due to numerical noise, and hence $\sigma_{\mathscr{A}}$ is reduced when a large number of computational particles and a proper particle loading are employed.

In all simulations, the plasma radial profile is Gaussian, with r.m.s. $R_w/4$ (cf. Fig. A.1), and typical physical parameters have been adopted, for which relevant drive-induced density fluctuations were observed in the experiments [1] (drive amplitude 0.4 V, drive frequency variable in the range 3.5–2 MHz with sweep rate 5×10^{10} Hz/s, plasma temperature 6 eV and a total charge of 4×10^8 electrons). The results show that the response of the system is very low when a single radial zone is employed ($N_R = 1$), independently of the number of computational particles. In this case, the excitation of the system is ineffective and no coherent structures are induced in the simulation. The situation drastically improves when $N_R = 2$, and the response is almost independent on N_R when $N_R \geqslant 4$ (this is verified even for the lowest value of N_P). Moreover, for $N_R \geqslant 3$, the mean response is almost identical with $N_P = 7.5 \times 10^4$, 1.5×10^5, and 3×10^5, even though, as expected, an increase in the number of computational particles leads to a decrease in $\sigma_{\mathscr{A}}$. Thus, an accurate analysis of the formation and evolution of the nonlinear structure can be achieved with a low number of radial zones, even with modest numbers of computational particles per radial zone, at a computational cost which is comparable to that of a standard one-dimensional PIC code.

To further analyze the dependence of the results on N_R and N_P, the quantity $\langle \mathscr{A} \rangle$ has been measured for different sweep rates (varying in the range 4–8×10^{10} Hz/s), with identical drive amplitude and initial and final drive frequencies. This range of sweep rates has been properly chosen in order to contain the threshold beyond which no large fluctuations can be induced in the experiment [1,14]. The results are shown in Fig. 9: curve (a) plots the behavior of $\mathscr{A}$ for a set of simulations with $N_R = 5$ and a large number of computational particles ($N_P = 3 \times 10^5$) which can be regarded as reference. Then, the same cases have been simulated with the same N_R, but with $N_P = 6 \times 10^4$ (curve *b*): the remarkable agreement between the two sets of data proves, again, that the present algorithm properly accounts for the important two-dimensional features of the problem with a low computational effort. On the other hand, the response of the system when only one radial zone is considered is reported in curve *d*, for $N_P = 3 \times 10^5$: in this case, the level of the response of the system is very low, no real excitation occurs and the presence of the threshold in the plasma excitation (observable for $N_R \geqslant 2$, see curves a–b–c) is lost. According to the single-zone approximation, the actual plasma radial profile is

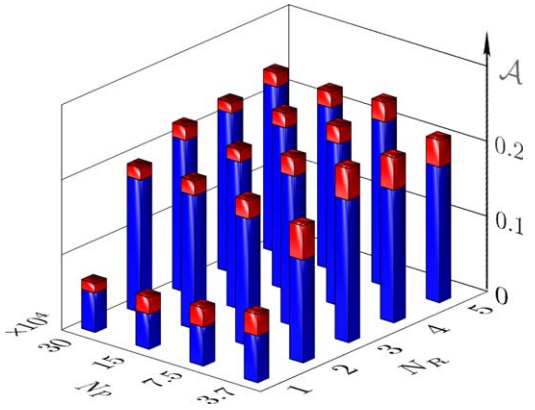

Fig. 8. Histogram of the amplitude $\mathscr{A}$ of the final response of the system, as function of the number N_R of radial zones and of the number N_P of computational particles. The upper part of each bar indicates the interval $(\langle \mathscr{A} \rangle - \sigma_{\mathscr{A}},\ \langle \mathscr{A} \rangle + \sigma_{\mathscr{A}})$.

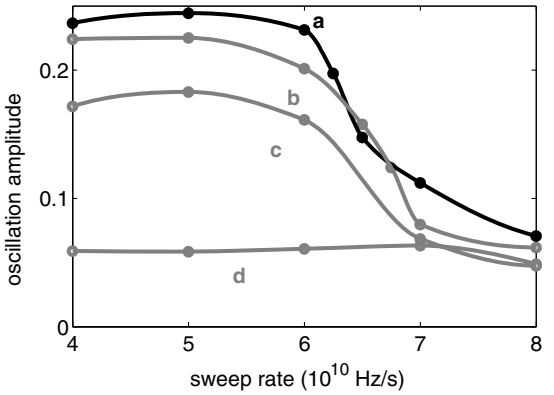

Fig. 9. Curves reporting the final amplitude of the density fluctuations as a function of the sweep rate, with a fixed drive amplitude of 0.4 V. The different curves refer to different approximations used in the code: (a) five radial zones, 6×10^4 computational particles per zone, $N_P = 3 \times 10^5$, (b) five radial zones, 1.2×10^4 particles per radial zone, $N_P = 6 \times 10^4$, (c) two radial zones, 1.5×10^5 particles per radial zone, $N_P = 3 \times 10^5$, and (d) one radial zone, $N_P = 3 \times 10^5$.

approximated with a flat profile of same total charge and the self-consistent field, which is primarily important in determining the response of the system [15], is strongly underestimated.

As the computational effort of the simulations is roughly proportional to the total number of computational particles, the results reported here show that N_R is primarily important in the simulations: in fact, if the real plasma profile is properly approximated, reliable results can be achieved even if relatively few particles are employed in each zone. On the other hand, if the approximation of the radial profile is excessively coarse, an increase in the number of computational particles does not lead to any significant improvement in the quality of the results.

6. Numerical studies of the BGK modes

In the simulations considered thus far, the driving conditions (drive amplitude, initial and final frequencies, sweep rate) were aimed at creating one large structure inside the plasma, consisting of a hole in phase-space. In all these cases, the large structure is generated by the fundamental harmonic of the drive potential. Nonetheless, higher spatial harmonics are present and are responsible for the generation of structures of smaller extent in phase space, which, in fact, are often seen to be absorbed by the larger one during the undriven evolution [14]. The typical phase-space portrait of the system at the end of the driven evolution is shown in Fig. 10, for the reference case discussed in the previous Section (see Fig. 8). The figures provide insight into the radial structure of the nonlinear mode, which is wider in velocity space at inner radii, but roughly of the same longitudinal extent at all radii. In particular, Fig. 10 shows that the $N_R = 1$ approximation does not lead to any significant excitation of the system, which is obtained only for $N_R \geqslant 2$. Nonetheless, the undriven evolution for $N_R = 2$ is different from the one obtained with $N_R = 5$. In fact, the numerical scheme slightly underestimates the mean velocity of the electron hole when $N_R = 2$, and a different phase (with respect to the reference case $N_R = 5$) is evidenced in the oscillations of the hole after 20 bounce periods. The phase difference decreases for $N_R = 3$, and becomes negligible for $N_R = 4$, proving that, in this case, the algorithm converges when only few radial zones are employed.

6.1. Interactions between BGK electron holes

An interesting study can be performed with this code concerning the interaction between structures of the same size. A simple way to induce the formation of two structures of the same size inside the plasma is doubling the drive frequency, without changing the sweep rate. In this way, the region of the Maxwellian distribution having $v \simeq 3v_{\text{th}}$ is now resonant with the second spatial harmonics of the drive. The fundamental resonance, on the other hand, is far in the tail of the Maxwellian ($v \simeq 6v_{\text{th}}$) and does not play an important

role in the evolution of the plasma (unless large sweep ranges are considered). A typical example of the phase-space structure that can be induced in this manner in shown in Fig. 11, in which two structures of the same size and shifted by a half period are clearly evident.

The radial profile considered for these simulations is steplike (i.e., constant for $r < r_{max}$ and 0 elsewhere, being $r_{max} = R_w/4$). Simulations with one and two radial zones have been performed (Fig. 11(a) and (b), respectively) and, for this radial profile, a remarkable agreement between the two approximations is observed. This situation differs from the cases considered earlier, where finer radial decompositions were required, and this difference can be simply explained. The z-integrated profile of the plasma is flat, and hence identical to its discrete version (see Appendix A). Moreover, the radius of the plasma column is considerably smaller than the radius of the trap, and thus a purely one-dimensional model of the plasma (i.e., a single-zone model) should provide results in good agreement with more refined radial approximations.

The pattern induced in the axial profile of the plasma density by the presence of the two holes bouncing back and forth with opposite phases is plotted, as function of time, in Fig. 12(a) for the case of Fig. 11(a). The figure shows the wakes left by the two structures moving along the axis of the plasma column. In the figure, the pattern is also compared with that obtained for the case in which a single large structure has been induced in the plasma (Fig. 12(b)).

In Fig. 11, minor structures due to third-order resonances are also visible at the end of the driven evolution, shifted of 2/3 of bounce period from one another. As already reported in [14], these smaller structures are absorbed by the larger ones during the undriven evolution and are not observed in the phase-space picture of the system after nearly 60 bounce periods (Fig. 13). The procedure described above can be generalized for the generic nth harmonic, providing a potentially useful tool for manipulating in detail the phase space distribution.

6.2. Comparisons with the BGK theory

Some of the more important features of these nonlinear structures can have an effective theoretical interpretation in the context of the BGK theory for one-dimensional plasmas with spatially-varying electrostatic

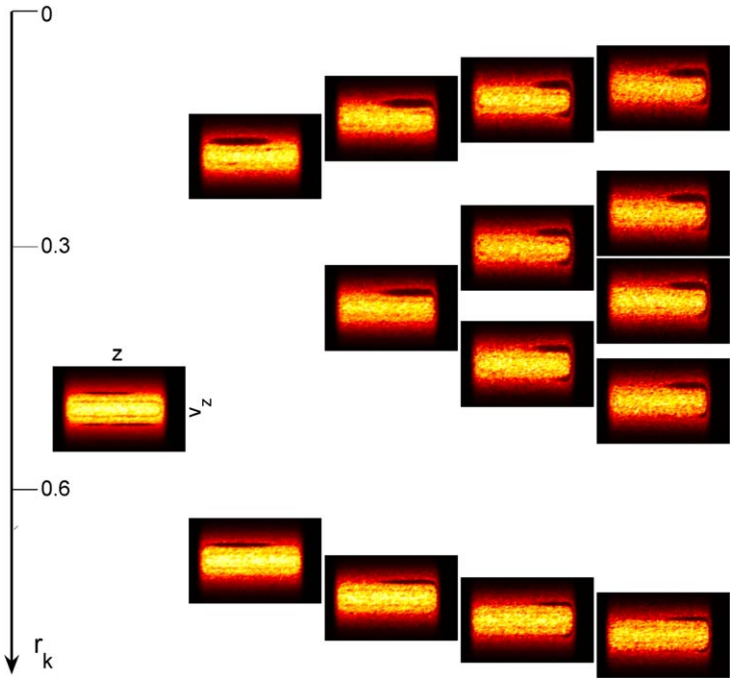

Fig. 10. Phase-space structure of the plasma after 20 undriven bounce periods, for the case discussed in Fig. 7 and for a number N_R of radial zones varying in the range 1–5.

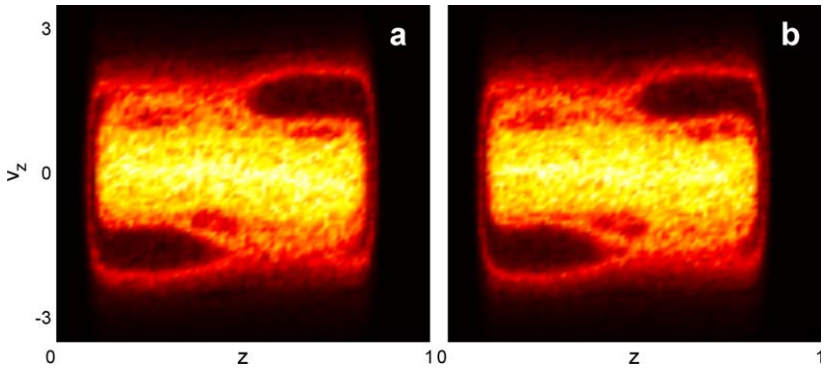

Fig. 11. Comparison between the phase-space structure of the plasma at the end of the driven evolution in the case of one radial zone (a) and two radial zones (b) (the area-weighed average of the two zones is reported). The plasma radial profile is steplike; the z-integrated density is constant for $r < R_w/4$ and 0 elsewhere. The electron density in the center of the trap is 1.8×10^{13} m^{-3}, for a total number of 4.2×10^8 particles. The drive is swept from 7 to 5 MHz, with a sweep rate of 5×10^{10} Hz/s and with amplitude of 0.5 V.

potentials [12]. According to the BGK theory, the phase-space distribution $f(z,v_z)$ in the reference frame of the hole can be written as $F^+(H(z,v_z))$ for $v_z > 0$ and $F^-(H(z,v_z))$ for $v_z < 0$, with H the electron axial Hamiltonian (see Eq. (30)). Moreover, $F^+(z,v_z)$ and $F^-(z,v_z)$ must be equal in the energy range of the trapped particles.

Before investigating the relation between the structures observed here and the BGK modes, one must recall that the classic BGK theory applies to infinite, homogeneous plasmas (ones that are not subjected to external potentials). For the plasmas considered here, the BGK theory is only expected to apply when the hole is in the central region of the trap (where the confining potential is negligible with respect to the self-potential) and only if the spatial width of the phase-space hole is reasonably smaller than the length of the plasma column. In this case, the hole may be regarded as immersed in an infinitely-long system. Moreover, due to the two-dimensional nature of the problem, one must expect different functions F^+, F^- at each radial layer (even though, due to the same mechanism of excitation, one must expect a similar behavior of the $F^{\pm}$s for different layers).

Here follows the analysis of the f-H correlation in the case where a phase-space hole of limited spatial extent is excited. The radial profile is steplike, with radius $r = R_w/4$, $N_R = 2$, and $N_P = 2 \times 10^5$; the driving potential

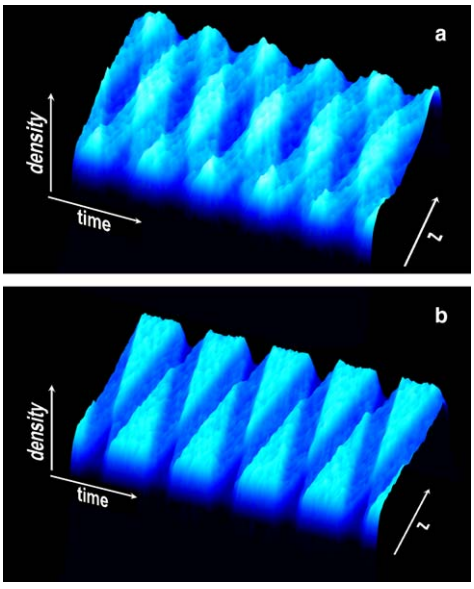

Fig. 12. Plot of the density pattern defined by the presence of two (a) and one (b) large holes.

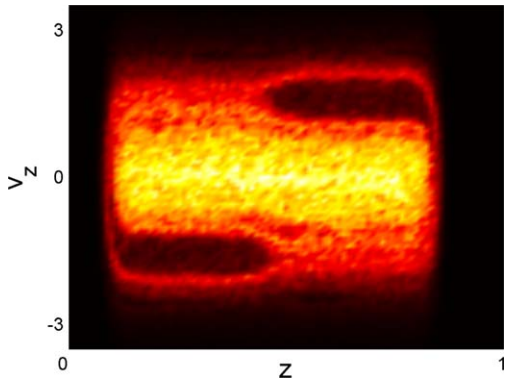

Fig. 13. Phase-space structure of the plasma for the case of Fig. 10(a), after 60 undriven periods. The smaller structures due to third-order resonances have disappeared, and only the two larger structures are evident.

has amplitude 0.5 V, and its frequency varies from 4 to 2.3 MHz with sweep rate 5×10^{10} Hz/s; the initial plasma temperature is 6 eV. At the end of the driving process the undriven evolution of the plasma is simulated, and the phase-space distribution is analyzed after 60 undriven bounce periods. In order to analyze their mutual relation, f and H have been evaluated over a suitable (z,v_z) grid for each radial zone, in the reference frame of the moving structure, considering a region of phase-space around the hole, in order to eliminate par-

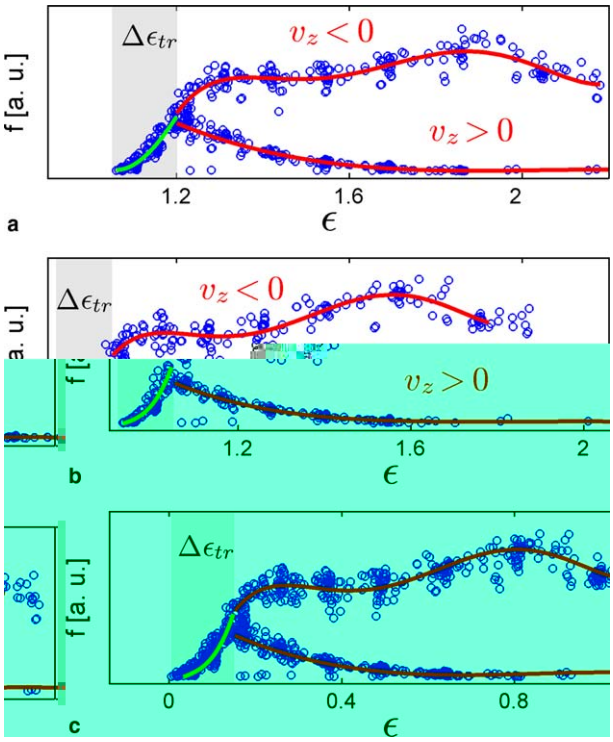

Fig. 14. Scatter plots showing the correlation existing between the electron distribution function f and the single-particle Hamiltonian H in the frame of reference of the moving structure, for the inner (a) and outer (b) radial zone. The different branches of the function $f(H(z,v_z))$, corresponding to $F^{\pm}$ in the trapped and untrapped energy ranges, are evident (the solid lines are obtained by best-fitting the data). The shaded regions mark the range of trapped energies. In the untrapped regime, the upper branch correspond to particles moving with negative velocity v_z in the frame of reference of the bucket (F^-), while the lower branch is associated with particles moving with $v_z > 0$ (F^+). Hence, the upper curve refers to the bulk of the Maxwellian, where the distribution function has its maximum value, while the lower curve refers to the tail of the distribution. (c) Scatter plot obtained by superimposing the scatter plots of (a) and (b) (a rigid shift of the abscissas is considered for both curves, in order to set the zero-energy level at the bottom of the potential well for the two radial zones).

ticles at the ends of the plasma column (where the external potential largely dominates) and avoid particles with energy ϵ_p too high with respect to the range of energies corresponding to trapped-particle trajectories. This has been done in order to properly resolve the energy range of trapped particles. The values of f and H obtained for the two zones are shown in Fig. 14(a) and (b). A strong correlation between f and H clearly exists, in close agreement with the classic BGK theory: in particular, the two branches of the scatter plot (which refer to untrapped energies) are seen to converge in the single branch that defines the range of trapped energies. As expected, the correlation is nearly the same for the two radial zones. In fact, one can see that the two sets of data look very similar but are shifted in energy (by an amount corresponding to the difference in the radially-averaged self-consistent potentials for the two radial zones in the center of the trap, equal to 0.15 in the considered units). If a shift in energy is considered (with the new zero-energy level at the bottom of the two potential wells), the two scatterplots of Fig. 14(a) and (b) can be superimposed, demonstrating the similar correlations for the two sets of data (Fig. 14(c)). The numerical results presented here provide considerable insights into the nature of these structures and confirm that, at least in the center of the trap, the phase-space distribution is the one predicted by the BGK theory.

7. Conclusions

It has been shown that a novel particle loading technique can be used to greatly reduce PIC simulation noise in a nonneutral plasma simulation and that a fully two-dimensional PIC code is not needed to study such plasmas in the azimuthally symmetric and highly magnetized limits considered here. A sophisticated physical phenomenon, the autoresonant excitation and control of BGK modes, was studied with a PIC code that implemented these ideas. The numerical algorithm can be employed on machines of modest computational performance and produces results of high precision. The key ideas are: (1) a decomposition of the fully two-dimensional problem into a set of few, coupled one-dimensional systems, which preserves a high precision in the evaluation of the self-consistent electrostatic potential; (2) an accurate particle loading (uniformly in phase, on curves of constant particle action in the equilibrium plasma), which allows for a significant reduction of numerical noise, even when employing reasonably low numbers of computational particles. In principle, both algorithms may prove useful for other problems in computational plasma physics, when a trade-off between computational cost and accuracy has to be determined.

Acknowledgement

One of the authors (J.W.) thanks the support of the Division of High-Energy Physics, USDOE.

Appendix A

For a generic, fixed number N_R of radial zones, the criterion chosen in the decomposition of the plasma radial profile is based on the minimization of the quantity I_{N_R}, defined as

$$I_{N_R} = \frac{\int [\sigma(r) - \tilde{\sigma}_{N_R}(r)]^2 r \, \mathrm{d}r}{\int \sigma^2(r) r \, \mathrm{d}r}, \tag{A.1}$$

where $\sigma(r)$ is the actual radial profile of the z-integrated plasma density and $\tilde{\sigma}_{N_R}(r)$ its approximation by means of N_R radial zones,

$$\tilde{\sigma}_{N_R} = \sum_{k=1}^{N_R} \sigma_k b_0 \left(\frac{r - r_k}{\Delta r_k} \right). \tag{A.2}$$

The quantity I_{N_R} is the total, area-weighted normalized quadratic error which is introduced when the discretized radial profile is considered. I_{N_R} is a function of the $2N_R - 1$ parameters which have yet to be determined, namely, the N_R values $\{\sigma_k\}$ (i.e., the values of $\tilde{\sigma}_{N_R}(r)$ on the different radial zones) and the $N_R - 1$ radii $\{R_k\}$ delimiting the different radial zones. The R_ks are defined such that $r_k = (R_k + R_{k+1})/2$ and $\Delta r_k = R_k - R_{k-1}$, with $R_1 = 0$, $R_{N_R} = R_w$. By minimizing I_{N_R}, one obtains the nonlinear set of equations:

$$\begin{cases} \sigma_k = \dfrac{1}{r_k \Delta r_k} \displaystyle\int_{\Delta r_k} \sigma(r) r \, \mathrm{d}r, \quad k = 1, \ldots, N_R, \\ \sigma(R_k) = \dfrac{\sigma_k + \sigma_{k+1}}{2}, \quad k = 1, \ldots, N_R - 1, \end{cases} \tag{A.3}$$

where the first of Eq. (A.3) shows that the procedure is charge-preserving. The system (A.3) can be solved iteratively with simple procedures. Fig. A.1 plots the results for a Gaussian radial profile of r.m.s. equal to $R_w/4$, for different values of N_R.

According to the procedure described above, a generic plasma profile is approximated at lowest order (i.e., with a single radial zone) with a uniform profile, covering the entire transverse section of the trap. Sometimes, this may provide a somewhat coarse description of the actual radial profile, especially for situations in which the typical radius of the plasma is significantly smaller than the radius of the trap (see, for instance, the case reported in Fig. A.1). In such cases, the procedure can be improved furtherly, in order to provide a better representation of the radial profile with a reduced computational cost, by imposing that the density in the last layer to be zero. In general, if N_R "computational" zones are to be considered, the procedure described above is now employed for $N_R + 1$ zones. The minimization of the same functional I_{N_R} is calculated, imposing the density in the outer zone to be zero and with the extra constraint given by the conservation of the total charge in the system. In this way, even if $N_R + 1$ zones have been employed in the discretization of the plasma profile, no computational particles are positioned in the last zone, and the effective number of radial zones employed in the PIC calculations is N_R. By using the method of the Lagrangian multipliers, one obtains:

$$\begin{cases} \sigma_k = \dfrac{\int_{\Delta r_k} \sigma(r) r \, \mathrm{d}r}{(1-\lambda) r_k \Delta r_k}, \quad k = 1, \ldots, N_R, \\ \sigma(R_k) = \dfrac{\sigma_k + \sigma_{k+1}}{2} - \lambda, \quad k = 1, \ldots, N_R - 1, \\ \lambda = \dfrac{\int_{R_{N_R-1}}^{R_w} \sigma(r) r \, \mathrm{d}r}{\int_0^{R_w} \sigma(r) r \, \mathrm{d}r}. \end{cases} \tag{A.4}$$

According to the new procedure, if a plasma distribution of characteristic radius well below R_w is considered, the $N_R = 1$ approximation leads to a steplike distribution of radius well below the radius of the trap, thus providing a better representation of the plasma profile with a single radial zone. This can also be seen by analyzing the data in the Table A.1: the table contains the value of the minimized functional I_{N_R} with the optimization procedures defined by Eq. (A.3) ($I_{N_R,1}$, second column) and Eq. (A.4) ($I_{N_R,2}$, third column). The data refer to

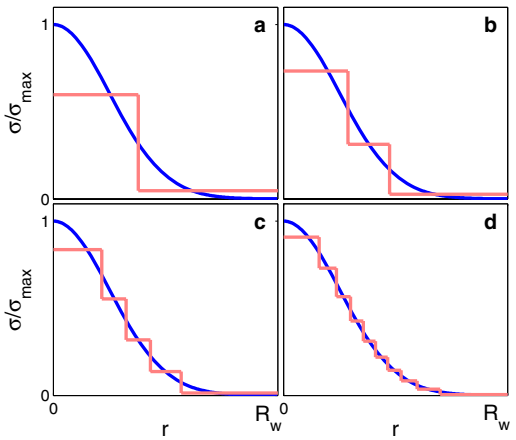

Fig. A.1. Determination of the stepwise radial profile of Eq. (A.2), to be used in the PIC simulations, starting from a continuous, Gaussian radial profile of r.m.s. equal to $R_w/4$. The stepwise profile has been obtained by solving the system of Eq. (A.3), for (a) 2, (b) 3, (c) 5 and (d) 10 radial zones.

Table A.1
Values of the functional I_{N_R} after minimization with the two different procedures of Eq. (A.3) ($I_{N_R,1}$, second column) and of Eq. (A.4) ($I_{N_R,2}$, third column)

N_R	$I_{N_R,1}$	$I_{N_R,2}$
1	7.49×10^{-1}	2.87×10^{-1}
2	1.59×10^{-1}	1.07×10^{-1}
3	6.69×10^{-2}	5.47×10^{-2}
4	3.68×10^{-2}	3.29×10^{-2}
5	2.31×10^{-2}	2.20×10^{-2}
6	1.60×10^{-2}	1.57×10^{-2}
7	1.16×10^{-2}	1.17×10^{-2}
8	8.90×10^{-3}	9.12×10^{-3}
9	6.98×10^{-3}	7.30×10^{-3}
10	5.63×10^{-3}	5.95×10^{-3}

N_R (first column) is the number of radial zones effectively considered in the PIC calculations.

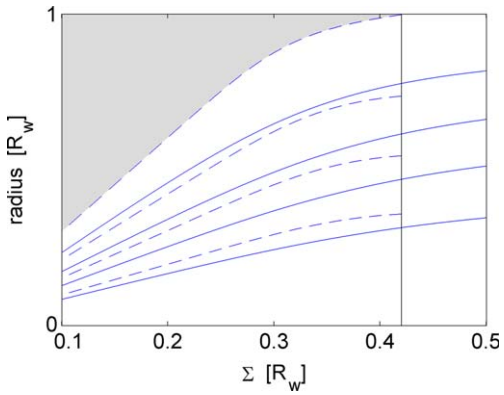

Fig. A.2. Plot of the radii delimiting the different radial zones, according to the procedure defined in Eq. (A.3) (solid lines) and Eq. (A.4) (dashed lines). In the figure, the shaded region indicates, for all the Σs, the outer radial zone in which, according to the second optimization procedure, the plasma density is set to zero. The vertical line shows that the second procedure can be successfully employed for a Gaussian profile only for $\Sigma < 0.42$, beyond which unphysical results are obtained. This proves that the second procedure can be useful only for radial profiles of characteristic radius well below the radius of the trap.

the Gaussian profile of Fig. A.1. In the table, N_R (first column) is the number of radial zones effectively considered in the PIC calculations, i.e., the radial zones in which the piecewise-constant density coming from the minimization procedure is different from zero.

Finally, the two procedures can be compared by observing, in Fig. A.2, the radii delimiting the different radial zones obtained in the two ways, for $N_R = 5$ with the first procedure and $N_R = 4$ for the second one (in order to consider the same number of radial zones in the discretization of the radial profile). Gaussian profiles are considered, with r.m.s., Σ, varying in the range $(0.1\text{–}0.3)R_w$.

References

[1] W. Bertsche, J. Fajans, L. Friedland, Phys. Rev. Lett. 91 (2003) 265003.
[2] J.R. Danielson, F. Anderegg, C.F. Driscoll, Phys. Rev. Lett. 92 (2004) 245003-1.
[3] J. Fajans, E. Gilson, L. Friedland, Phys. Rev. Lett. 82 (1999) 4444.
[4] J. Fajans, E. Gilson, L. Friedland, Phys. Plasmas 6 (12) (1999) 4497.
[5] J. Fajans, L. Friedland, Am. J. Phys. 69 (10) (2001) 1096.
[6] J.M. Malmberg, C.F. Driscoll, B. Beck, D.L. Eggleston, J. Fajans, K. Fine, X.P. Huang, A.W. Hyatt, in: C. Roberson, C. Driscoll (Eds.), Nonneutral Plasma Physics, vol. 175, AIP, New York, 1988, p. 28.
[7] K.S. Fine, Phys. Fluids B 4 (1992) 3981.
[8] J.M. Finn, D. del-Castillo-Negrete, D.C. Barnes, Phys. Rev. Lett. 84 (2000) 2401–2404.

[9] G.G.M. Coppa, A. D'Angola, G.L. Delzanno, G. Lapenta, Phys. Plasmas 8 (4) (2001) 1133.
[10] E. Gilson, J. Fajans, Quadrupole induced resonant particle transport in a pure-electron plasma, Phys. Rev. Lett. 90 (2003) 015001.
[11] J. Fajans, A. Schmidt, Malmberg–Penning and minimum-B trap compatibility: the advantages of higher-order multipole traps, Nucl. Instr. Meth. A 521 (2004) 318.
[12] I.B. Bernstein, J.M. Greene, M.D. Kruskal, Phys. Rev. 108 (1957) 546.
[13] G.W. Mason, R.L. Spencer, Simulations of the instability of the $m = 1$ self-shielding diocotron mode in finite-length non-neutral plasmas, Phys. Plasmas 9 (2002) 3217.
[14] F. Peinetti, W. Bertsche, J. Fajans, J. Wurtele, L. Friedland, Phys. Plasmas 12 (2005) 062112.
[15] L. Friedland, F. Peinetti, W. Bertsche, J. Fajans, J. Wurtele, Phys. Plasmas 11 (2004) 4305–4317.
[16] C.K. Birdsall, A.B. Langdon, Plasma Physics via Computer Simulation, McGraw-Hill, New York, 1985.
[17] L. Silva, M. Marti, J.R. Davies, R.A. Fonseca, C. Ren, F.S. Tsung, W.B. Mori, Phys Rev Lett. 92 (2004) 015002.